ЖЭТФ, 2024, том 166, вып. 2 (8), стр. 261–276

UNTANGLING THE VALLEY STRUCTURE OF STATES FOR INTRAVALLEY EXCHANGE ANISOTROPY IN LEAD CHALCOGENIDES QUANTUM DOTS

I. D. Avdeev**, *M. O. Nestoklon

Ioffe Institute of the Russian Academy of Sciences
194021, Saint Petersburg, Russia

Received March 4, 2024,
revised version March 28, 2024,
Accepted for publication March 29, 2024

We put forward a generalized procedure which allows to restore the bulk-like electron and hole wave functions localized in certain valleys from the wave functions of quantum confined electron/hole states obtained in atomistic calculations of nanostructures. The procedure is applied to the lead chalcogenide quantum dots to accurately extract the intravalley velocity matrix elements and the constants of the effective intravalley Hamiltonian of the exchange interaction for the ground exciton state in PbS and PbSe quantum dots. Our results suggest that intravalley parameters in PbS quantum dots are much more anisotropic than the ones in PbSe. Renormalization of the velocity matrix elements, forbidden band gap, valley and exchange splittings of exciton and exciton binding energy are also calculated.

DOI: 10.31857/S0044451024080121

1. INTRODUCTION

Currently, semiconductor-based nanostructures are widely used for various applications. In particular, quantum dots (QDs) [1] offer the tunability of various properties from the basic ones like the effective band gap to more complicated such as exchange interaction in excitons [2] and carrier g-factor values [3, 4]. Rapid progress of experimental techniques demands for the detailed theoretical insight into properties of semiconductor nanostructures. However, until now there is a gap between purely phenomenological methods based on the $\mathbf{k}\cdot\mathbf{p}$ model [5,6] and atomistic calculations, both empirical [7,8] and *ab initio* [9,10]. For the band structure calculations, the interpretation of the atomistic results within the $\mathbf{k}\cdot\mathbf{p}$ framework is straightforward. For nanostructure calculations in most cases additional work has to be done. Observable quantities (splitting energies, optical matrix elements, etc.) are available directly from the atomistic calculations. However, their values typically results from the complex interplay of conceptually different phenomena (mixing of the states at interfaces, anisotropy of effective masses, exchange interaction, etc.). For the qualitative description and prediction of physical properties of real nanosystems the values of interest are usually the latter ones.

Particularly complex problem is the fine energy structure of the nanostructures of multi-valley semiconductors (e. g. lead chalcogenides, Si, Ge), where such values of interest are blended by the mixing of the valley states. In simple cases, such as SiGe quantum wells [11, 12] or [110]-grown PbX nanowires with the simple surface [13], straightforward parametrization of the valley splitting is possible. Though, in most cases the valley mixing can be taken into account only phenomenologically. In this work we focus on lead chalcogenides and propose a generalized solution to this problem.

Lead chalcogenides PbX, X=S, Se are narrow direct band gap semiconductors suitable for infrared optoelectronic applications [14–16] due to the tunability of the band gap in a wide range of the infrared spectrum. Under normal conditions they have the rock-salt crystal structure with O_h^5 space group and complex multivalley band structure. Conduction and valence band extrema in PbX are located at the four inequivalent anisotropic L valleys.

As a result of the broken translational symmetry in lead chalcogenide quantum dots (nanostructures) different L valley states are mixed and the carriers wave

* E-mail: ivan.avdeev@mail.ioffe.ru

functions are the combinations of the pure valley states [17–19]. The valley mixing spreads the local density of states in k-space among all the L valleys [18] and makes it difficult to map the atomistic calculations onto the effective model and vice versa [19]. In particular, the very complex fine structure of the excitons stems from the interplay of spin-orbit splitting, valley-mixing and exchange interaction [19]. This also results in complex behaviour of carriers' g-factors [3]. The second mechanism responsible for the lifting of the valley degeneracy is the anisotropy of effective masses. The disentanglement of different contributions to the exciton fine structure is further complicated by the strong anisotropy of effective masses in PbX [17, 20] which is, however, can be captured successfully in the framework of the effective $\mathbf{k}\cdot\mathbf{p}$ theory, see, e.g., Refs. [21–23].

Below we present our solution of how to trace the valley structure of the ground electron (hole) states in PbX QDs from atomistic calculations to enable direct mapping onto analytical models. The proposed procedure relies on the symmetry analysis and computation of the local density of states in reciprocal space at the four inequivalent L points in the Brillouin zone. As an example we use the obtained pure valley states to calculate the intravalley anisotropic exchange constants and intravalley interband velocity matrix elements in cubic, cuboctahedral and octahedral PbX quantum dots with tetragonal symmetry, similar to the ones studied in Ref. [19].

We demonstrate that these quantities are almost insensitive to the shape of the quantum dot and agree very well with effective mass calculations. Direct access to the valley states allows us to show that velocity and exchange Coulomb matrix elements in PbS quantum dots are much more anisotropic than in PbSe in the considered range of quantum dot diameters from 3 nm to 25 nm.

2. VALLEY STATES

In bulk PbX crystal the valley states are the electron and hole states at the band extrema located at the four inequivalent independent L valleys. In each valley the states are classified by irreducible representations of the L valley wave vector point group D_{3d} [18]. This group has six spinor representations: two two-dimensional $\Gamma_4^{\mp}$ and four one-dimensional conjugated $\Gamma_5^{\mp}$ and $\Gamma_6^{\mp}$ in Koster's notation [24]. These representations are also known as $L_6^{\mp}$, $L_4^{\mp}$ and $L_5^{\mp}$ respectively [25]. (Hereafter throughout the paper we use only the Koster's notation.) Since the one dimensional representations $\Gamma_5^{\mp}$ and $\Gamma_6^{\mp}$ are conjugated (related by time inversion) they also form doubly degenerate energy levels $\Gamma_5^{\mp} \oplus \Gamma_6^{\mp} \equiv \Gamma_{56}^{\mp}$.

2.1. Extended effective mass model

In PbX crystal the ground conduction band edge states are odd and transform according to Γ_4^- (L_6^-), while the ground valence band edge states are even and form the basis of Γ_4^+ (L_6^+) [26]. The center of inversion is assumed to be at cation. The standard basis functions of $\Gamma_4^{\pm}$ are (pseudo)spinors [24], therefore we refer the band edge states at the L valleys as the valley (pseudo)spinors

$$\boldsymbol{\mathcal{E}}^b_\mu = (|b,\mu,\uparrow\rangle, |b,\mu,\downarrow\rangle), \tag{1}$$

where $b = c, v$ or «−»,«+» is the band index, $\mu = 0, 1, 2, 3$ is the valley index and $\uparrow, \downarrow$ are the indices of (pseudo)spins oriented along the valley axis. Due to the O_h rotational symmetry of the bulk PbX crystal the valley (pseudo)spinors in different valleys are not fully independent. Indeed, for any $g \in O_h$ the functions $g\boldsymbol{\mathcal{E}}^b_\mu \equiv \boldsymbol{\mathcal{E}}^b_{\mu'}$ are also eigenstates of the bulk Hamiltonian with same energy E^b, but some at different L valley $g\mathbf{k}_\mu \equiv \mathbf{k}'_\mu$. This allows us to construct the valley (pseudo)spinor basis

$$\boldsymbol{\mathcal{E}}^b_{VP} = (\boldsymbol{\mathcal{E}}^b_0, \boldsymbol{\mathcal{E}}^b_1, \boldsymbol{\mathcal{E}}^b_2, \boldsymbol{\mathcal{E}}^b_3) \tag{2}$$

of the irreducible star of L valleys with known transformation properties

$$g\boldsymbol{\mathcal{E}}^b_{VP} = \boldsymbol{\mathcal{E}}^b_{VP} D^b(g). \tag{3}$$

We refer it as the ground valley multiplets. The transformation matrices of $\boldsymbol{\mathcal{E}}^b_{VP}$ can be established explicitly by choosing specific rotations $g_\mu \in O_h$ to relate the valley states in different valleys, such as $\boldsymbol{\mathcal{E}}^b_\mu = g_\mu \boldsymbol{\mathcal{E}}^b_0$. Possible choices for g_μ are either the powers of S_{4z} rotoreflection [19], powers of C_{4z} [27] or C_{2x}, C_{2y} and C_{2z} rotations [3].

When nanostructured the translation symmetry is broken and the eightfold degenerate ground valley multiplets (2) split into several energy levels. The number of levels and their symmetries are determined by decomposition of the transformation matrices $D^b(g)$, Eq. (3), into irreducible representations of the symmetry group of the quantum dot (nanostructure). Decomposition of the D^b matrices is given by symmetrization matrices S^b via ${S^b}^{-1} D^b S^b$. The S^b matrices are chosen in such a way so the new basis $\boldsymbol{\mathcal{E}}^b_{VP} S^b = \boldsymbol{\mathcal{E}}_P$

$$\sum_{\mu=0}^{4} \sum_{\eta=\uparrow,\downarrow} |b,\mu,\eta\rangle\, S^b_{\mu\eta,\Gamma_i F_z} = |b,\Gamma_i,F_z\rangle \tag{4}$$

transforms as (pseudo)spin. Here $|b, \Gamma_i, F_z\rangle$ are the states which transform as the standard basis functions [24] of the irreducible representation Γ_i. Several S matrices for [111]-nanowires with D_{3d} point group and QDs with T_d symmetry were calculated in Refs. [3,18,19]. In quantum dots (nanostructures) the symmetry of the ground valley multiplets holds. Indeed, the bulk states may be related to the states in nanostructures in the two-step procedure: (i) formation of combinations of bulk states into states which transform under representations of nanostructure symmetry group and (ii) renormalization of energies of these states due quantum confinement (localization in r-space and delocalization in k-space, see [5]).

2.2. Empirical tight-binding method

For atomistic calculations of PbX quantum dots (nanostructures) we use the $sp^3d^5s^*$ nearest neighbour variant of the tight-binding method [17]. In this model the electron and hole wave functions are expanded over the basis of Löwdin orbitals $|n\xi\rangle$ [28] localized near atomic sites

$$|\Psi\rangle = \sum_{n\xi} C_{n\xi} |n\xi\rangle . \tag{5}$$

Here ξ describes both spin and one of the s, p, d or s^* type of the orbital, n is the atomic site index. Coefficients $C_{n\xi}$ are obtained via numerical diagonalization of the tight-binding Hamiltonian, which is represented by a large sparse matrix

$$\hat{H} = \sum_{n\xi n'\xi'} H_{n'\xi' n\xi} |n'\xi'\rangle \langle n\xi| . \tag{6}$$

In the nearest neighbour approximation there are up to $7 \cdot 2^2 \cdot 10^2 \cdot N_a$ nonzero elements in the matrix, where $7 = 6 + 1$ is the maximal number of nearest neighbours $n \neq n'$ plus diagonal $n = n'$, 2 is the number of spins, 10 is the number of the $sp^3d^5s^*$ orbitals and N_a is the number of atoms in the quantum dot (nanostructure).

Numerical diagonalization of the tight-binding Hamiltonian is performed using the thick-restart Lanczos algorithm [29,30]. This is efficient iterative method which has linear computational complexity $\mathcal{O}(m \cdot N_a)$ of finding exactly m eigenvectors near the band gap. Due to the Kramers symmetry the electron (hole) energy levels E_i are doubly or quadruple degenerate depending on the point symmetry of the quantum dot (nanostructure). There is some randomness in degenerate tight-binding eigenstates $|i, p\rangle$ ($p = 1, \ldots, n_i$) of Eq. (6)

$$\hat{H} |i, p\rangle = E_i |i, p\rangle \tag{7}$$

since any linear combination of degenerate states is also an eigenstate with the same energy E_i. For each energy level E_i these states $\boldsymbol{\mathcal{E}}_i = (|i, 1\rangle, \ldots, |i, n_i\rangle)$ form a basis of an irreducible representation Γ_i of size n_i. Therefore we can define the *symmetrized* states $|\Gamma_i, F_z\rangle$ as

$$\sum_p |i, p\rangle V^i_{p,F_z} = |\Gamma_i, F_z\rangle , \tag{8}$$

where V^i is a unitary matrix and $|\Gamma_i, F_z\rangle$ are the (pseudo)spin-like states with standard transformation properties [24]. Eq. (8) is readily generalized to any number of energy levels

$$\boldsymbol{\mathcal{E}}_{TB} V = \boldsymbol{\mathcal{E}}_P, \tag{9}$$

where $\boldsymbol{\mathcal{E}}_{TB} = (\boldsymbol{\mathcal{E}}_1, \ldots, \boldsymbol{\mathcal{E}}_n)$ is the set of sets of tight-binding states with energies $E_1, \ldots, E_n$, $\boldsymbol{\mathcal{E}}_P = (\boldsymbol{\mathcal{E}}_{\Gamma_1}, \ldots, \boldsymbol{\mathcal{E}}_{\Gamma_n})$ is the set of sets of symmetrized states with standard transformation properties. The matrix $V = \mathrm{diag}(V_1, \ldots, V_n)$ is block-diagonal. Accidental degeneracy of states $E_i = E_j, i \neq j$ is not considered as may be removed by small perturbation.

2.3. Mapping tight-binding results to effective mass model

The next step is to identify the states of the split conduction and valence band ground valley multiplets in atomistic calculations. In most cases they are simply eight closes to the band gap states in each band. However, a situation when the distance between quantum confined levels is smaller than the splittings of the valley multiples is possible [18]. For such extreme case the states of the ground valley multiplets can be identified in k-space. As shown in Ref. [18] the ground electron and hole states have the maximum of local density in k-space exactly at the L points of the Brillouin zone, while the maximum of excited states is slightly displaced. In centrosymmetric quantum dots (nanostructures) excited states can be also distinguished by their opposite parity.

Finally, we define the conduction (valence) band valley states in PbX quantum dots (nanostructures) by combining Eqs. (4) and (8). In the matrix form it reads as

$$\boldsymbol{\mathcal{E}}^b_{VP} S^b = \boldsymbol{\mathcal{E}}^b_{TB} W^b, \tag{10}$$

where $\boldsymbol{\mathcal{E}}^{c(v)}_{TB}$ are the raw conduction (valence) band tight-binding states and $\boldsymbol{\mathcal{E}}^b_{VP}$ are the corresponding valley multiplets similar to Eq. (2). Instead of V^b, Eq. (8), we introduce a matrix W^b to account for possible uncertainties of the raw states to enable the inverse transformation to the basis of valley (pseudo)spinors given by

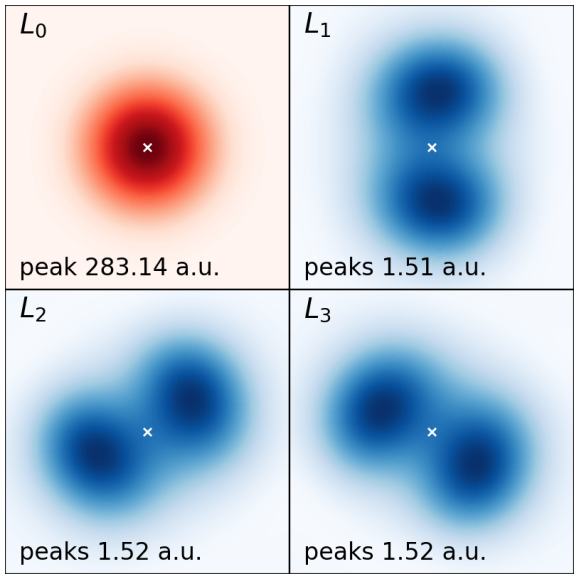

Fig. 1. Local density in the k-space of the same $|c, 0, \uparrow\rangle$ valley state in the Brillouin Zone surface near L valleys. The exact positions of the L_μ valleys are indicated by white «×». The main peak near L_0 valley (upper left) is shown in red colours, while the peaks near the other valleys L_1, L_2, L_3 are shown by blue colours with different scale of the colormap. The values (arb. units) of the maximal peak near each valleys are also indicated on the plots

$$U^b = W^b S^{b^{-1}}. \tag{11}$$

We factorize the matrix W (the band index is omitted for brevity) into three matrices

$$W = VPR, \tag{12}$$

where $V = \mathrm{diag}(V_{i_1}, \ldots, V_{i_N})$, Eq. (8), brings the tight-binding states to the (pseudo)spin form, the matrix P arranges the order of irreducible representations and accounts for the phases of their bases and the matrix R describes the possible rotation between repetitive irreducible representations in the decomposition of the valley multiplet. The matrix V can be computed as a sum over the point group of the quantum dot (nanostructure) as described in Appendix 4. The extra matrix P traces the permutations and phase multipliers for the irreducible representations in the decomposition, see details in Appendix 4. Parametrization of the R matrix is given in Appendix 4. The unknown phases and rotation angles for P and R matrices for the ground valley multiplets can be obtained by the numerical maximization of the local density of states in k-space at the four L points of the Brillouin zone.

To demonstrate the procedure, we reconstruct the valley states in the small cuboctahedral PbS QD without inversion ($D \approx 3.2$ nm, $N = 4, M = 0$ in Ref. [19]).

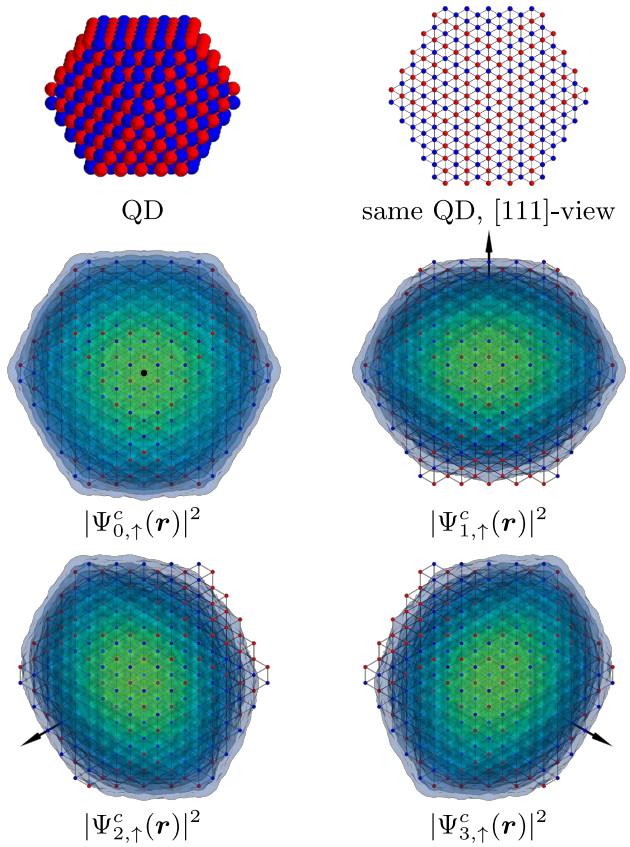

Fig. 2. [111]-view of the local densities in r-space of conduction band valley states $|c, \mu, \uparrow\rangle, \mu = 0, 1, 2, 3$ in the cuboctahedral QD shown at the top (for [111]-view the size of the atoms is reduced). The black arrows indicate the orientation of the corresponding L valleys

The arrangement of atoms in this QD is shown in the inset of Fig. 2. In tetragonal quantum dots the ground conduction and valence band valley multiplets split into two doublets $\Gamma_6 \oplus \Gamma_7$ and a quadruplet Γ_8. The only fitting parameters are three discrete phase multipliers for each band. As a result we obtain eight states $|b, \mu, \eta = \uparrow, \downarrow\rangle$ in each band $b = c(v)$ localized near L_μ valleys. The wave vectors of the L valleys are chosen as

$$\mathbf{k}_0 \parallel [111], \quad \mathbf{k}_1 \parallel [\bar{1}\bar{1}1], \quad \mathbf{k}_2 \parallel [1\bar{1}\bar{1}], \quad \mathbf{k}_3 \parallel [\bar{1}1\bar{1}]. \tag{13}$$

The 2D local density of the $|c, 0, \uparrow\rangle$ state in k-space near the L valleys is shown in Fig. 1. The part of the density near the L_0 valley is shown by red, while the density near other valleys are shown by blue with different scale. The scales of the colormaps are chose from 0 to the maximum of the local density in the corresponding cross section, which are indicated on the plots in arbitrary units. One can see that the main peak at

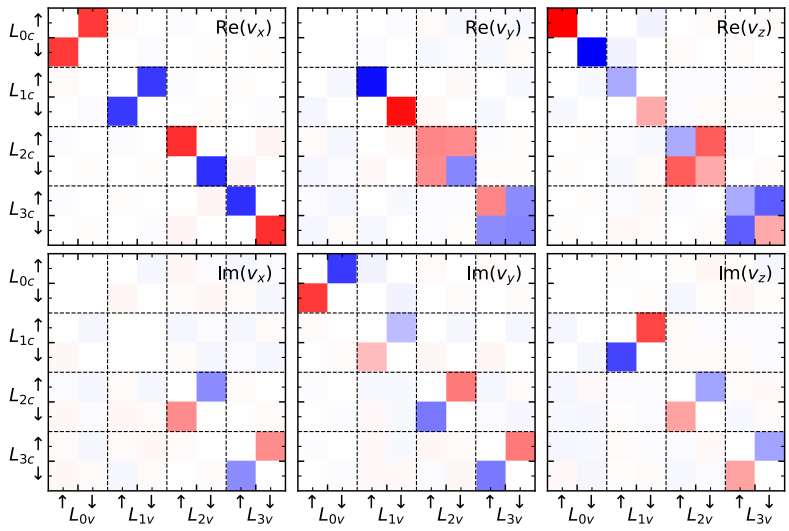

Fig. 3. Interband velocity matrix elements in the basis of valley state $\langle c, \mu, \eta\,|\hat{\mathbf{v}}|\,v, \mu', \eta'\rangle$ in the coordinate frame of the L_0 valley, Eq. (15), in QD with $D \approx 3.2$ nm (see text). Color encodes the amplitude of corresponding matrix elements

the L_0 valley is about 200 times larger than the peaks near other $L_\mu, \mu = 1, 2, 3$ valleys. Moreover, these 2D plots reveal the admixture of excited states at different valleys since the maxima of their density are misplaced from the L valleys. The positions of the L valleys in Fig. 1 are shown by small white «x» at the middle of each plot.

In Fig. 2 we also show the local density of all the valley states $|c, \mu, \uparrow\rangle$, $\mu = 0, 1, 2, 3$ in r-space. To emphasize the difference of the local densities of the valley states they are shown as projections onto the plane perpendicular to the [111] axis. In this plane projections of the effective masses in L_0 valley are isotropic, while projections of the other valleys L_μ, $\mu \neq 0$, are not. This results in the anisotropy in the projections of the local densities of the L_μ, $\mu = 1, 2, 3$, valley states, which is clearly seen in Fig. 2. The axis of this anisotropy depends on the projection of the corresponding L valley onto the (111) plane. The state at the L_0 valley is isotropic in this projection. The density of spin-down and valence band states look very similar.

3. RESULTS

We apply the developed method to unwind the valley structure of states in cubic, cuboctahedral and octahedral PbS and PbSe quantum dots with tetragonal symmetry T_d, similar to the ones studied in Ref. [19]. We show how having the explicit form of the valley multiplets helps to calculate physical properties of these quantum dots, such as interband velocity matrix elements and intravalley long range exchange Coulomb interaction, which otherwise are not directly accessible.

3.1. Interband velocity matrix elements

First we consider one of the simplest yet useful property of PbX quantum dots — interband velocity matrix elements $\langle c\,|\hat{\mathbf{v}}|\,v\rangle$ between the electron and hole ground levels. Velocity matrix elements in these quantum dots are computed as a commutator of of the tight-binding Hamiltonian with the coordinate operator, $\hat{\mathbf{v}} = i[\hat{H}, \mathbf{r}]/\hbar$ and we assume the diagonal approximation $\mathbf{r} = \delta_{mn}\delta_{\alpha\beta}\mathbf{r}_n$ where $\mathbf{r}_n$ is the coordinate of n-th atom [31]. Since the transformation of the tight-binding states to the valley (pseudo)spinors (10) given by the matrix U^b, $b = c, v$ (11), then the corresponding transformation of the velocity matrix elements is given by

$$\mathbf{V}_{VP} = U^{c\dagger}\mathbf{V}_{TB}U^{v}. \tag{14}$$

Result of this transformation is shown in Fig. 3 for the same $D \approx 3.2$ nm cuboctahedral PbS quantum dot, which atomistic structure is shown in inset of Fig. 2. In Fig. 3 the interband velocity matrix elements are given in the valley (pseudo)spin basis in the coordinates frame

$$n_{0x} \parallel [1\bar{1}0], \quad n_{0y} \parallel [11\bar{2}], \quad n_{0z} \parallel [111] \tag{15}$$

of the L_0 valley. Upper panels show real part of v_x, v_y, v_z (from left to right) components of the velocity matrix elements, lower panels show imaginary parts.

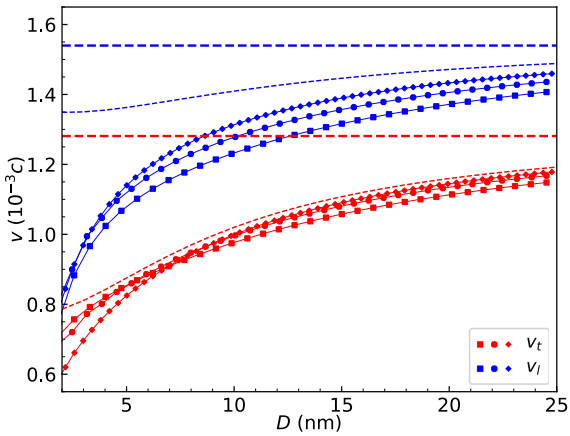

Fig. 4. Intravalley interband velocity matrix elements v_t, v_l in 10^{-3} speed of light in PbS QDs with different shapes as a function of effective QD diameter. Results of the tight-binding calculations are shown by symbols connected by thin solid lines. The shape of the symbols represent the shape of the QDs: cubic, cuboctahedral and octahedral. Results of the calculations in the framework of anisotropic k.p theory are shown by thin dashed lines. Dashed lines show the corresponding interband velocity matrix elements in the bulk crystal

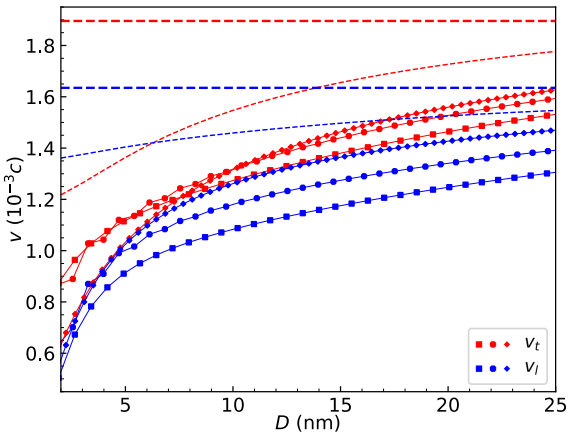

Fig. 5. Same as in Fig. 5 for PbSe QDs

The absolute values of velocity matrix elements are indicated by colour (positive by red, negative by blue, zero by white), the scale of the colormap is same for all the subplots. The upper left corner in each subplot correspond to the intravalley velocity matrix elements in the L_0 valley. One can clearly see that the spin matrices of the velocity operator in the L_0 valley are proportional to the Pauli matrices, $\hat{v}_i \propto \sigma_i$. The absolute values of the velocity matrix elements in L_0 valley, $v_x = v_y \neq v_z$, represent the internal anisotropy of the valley. One can also see there are traces of non-diagonal by the valley index optical transitions. The intervalley interband velocity matrix elements are non-zero due to the admixture to the ground valley states of excited states in other valleys seen in Fig. 1. This is a second order perturbation with respect to the valley splitting and it vanishes very quickly with increase of the size of the quantum dot (nanostructure).

The structure of the velocity matrix elements in the basis of valley states, Fig. 3, allows us directly calculate their values as

$$\begin{aligned} v_x &= \mathrm{Re}\,\langle c,0,\downarrow|\hat{v_x}|\,v,0,\uparrow\rangle\,, \\ v_y &= \mathrm{Im}\,\langle c,0,\downarrow|\hat{v_y}|\,v,0,\uparrow\rangle\,, \\ v_z &= \mathrm{Re}\,\langle c,0,\uparrow|\hat{v_z}|\,v,0,\uparrow\rangle\,. \end{aligned} \tag{16}$$

Results of the calculations are shown in Fig. 4 for PbS and in Fig. 5 for PbSe quantum dots in thousandths of the speed of light. Longitudinal ($v_l \equiv v_z$) intravalley interband velocity matrix elements are shown by blue, transverse ones ($v_t \equiv v_x = v_y$) by red. Tight-binding data are shown by symbols connected by thin solid lines for each of the three considered shapes of the quantum dots: cubic by «□», cuboctahedral by «○» and octahedral by «◇». For the detailed description of the atomistic structure and shapes of the quantum dots see Ref. [19]. Solid dashed lines show the corresponding velocity matrix elements in bulk PbS and PbSe crystals. Data calculated within the framework of fully anisotropic **k·p** model [3] are shown by thin dashed lines.

These plots, Figs. 4 and 5, reveal the scaling of the internal valley anisotropy in isotropic PbS and PbSe quantum dots. One can clearly see that velocity matrix elements almost insensitive to the shape of the quantum dots and converge to the corresponding values in bulk crystal at large diameters. Also these plots reveal that intravalley velocity matrix elements in PbSe quantum dots are almost isotropic in the range of diameters from about 5 nm to 15 nm, compared to to their PbS counterparts. Another interesting result is that anisotropic **k·p** theory for spherical quantum dots fails a bit to predict the scaling of the longitudinal component of the velocity at small diameters, especially for PbS.

3.2. Intravalley exchange interaction

The second application of the valley pseudospinors considered in this paper is the calculation of intravalley anisotropic long range exchange Coulomb interaction constants. These constant are calculated here for the same PbS and PbSe quantum dots as in Sec. 3.1 and Ref. [19].

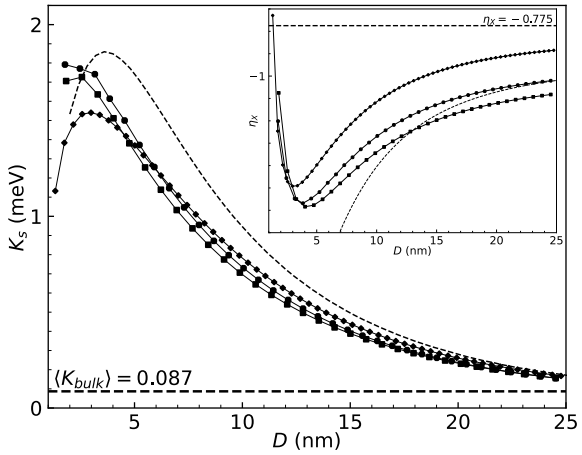

Fig. 6. In the main plot the averaged intravalley exchange constant K_s is shown as a function of QD diameter. Inset shows the intravalley exchange anisotropy parameter η_X as a function of QD diameter. Results of the tight-binding calculations are shown by symbols connected by thin solid lines. The shape of the symbols represent the shape of the QDs: cubic, cuboctahedral and octahedral. Results of the calculations in the framework of anisotropic $\mathbf{k}\cdot\mathbf{p}$ theory are shown by thin dashed lines. Thick dashed lines show the corresponding values in the bulk crystal (see Table 1)

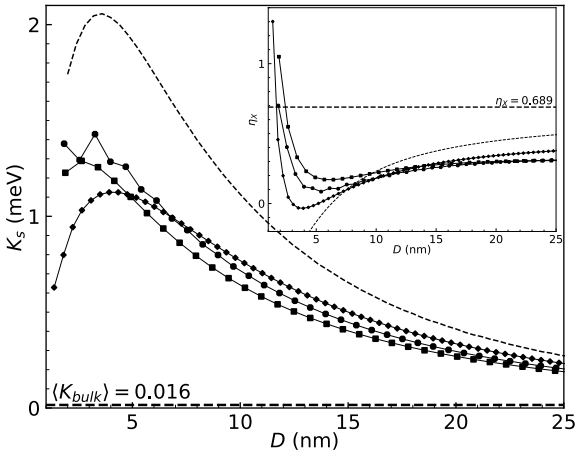

Fig. 7. Same as in Fig. 6 but for PbSe QDs

The problem with calculation of intravalley exchange interaction constants is the complicated interplay of intra- and intervalley Coulomb interaction and the valley mixing of electron, hole and exciton states. The full exciton Hamiltonian in PbX quantum dots has four main contributions

$$\hat{H}_X = \hat{H}_0 + \hat{H}_{VM} - \hat{J} + \hat{K}, \tag{17}$$

where $\hat{H}_0 \equiv E_g(D)\mathbb{1}$ describes the quantum confinement of electrons and holes, $\hat{H}_{VM}$ is the valley mixing, $\hat{J} \equiv J\mathbb{1}, J > 0$ is the direct Coulomb interaction and $\hat{K}$ is the long range exchange [19]. The quantum confinement and direct Coulomb are trivial diagonal parts of the Hamiltonian. The exciton fine structure is defined by the valley mixing $\hat{H}_{VM}$ and exchange interaction $\hat{K}$. It was shown in Ref. [19] that intra- and intervalley exchange are equally important and a phenomenological model for the exchange matrix $\hat{K}$ was proposed. The model is isotropic with one exchange constant $K(D)$ which can be calculated analytically. In this model the electron-electron representation of the long range exchange Hamiltonian in one L valley is

$$\hat{H}^{\rm iso}_{\rm exch} = K\left(\frac{\mathbb{1}}{2} - \frac{\boldsymbol{\sigma}^*\cdot\boldsymbol{\sigma}}{6}\right), \tag{18}$$

where K is the exchange constant and the spin matrix results from the angular parts of exchange integrals on the spherically symmetric electron and hole wave functions. The model also takes into account the valley splittings as external parameters and allows to calculate absorption spectrum of the ground exciton level which is then can be compared to the similar spectra in tight-binding. Comparison of the phenomenological model and tight-binding absorption spectra in PbS quantum dots was used in Refs. [19] and [32] to estimate the exchange constant in the tight-binding. The obvious drawback of this approach is that it requires a fitting procedure to minimize the difference between absorption spectra. This approach is not accurate.

In this work we calculate the intravalley exchange interaction constants straightforwardly fully taking into account the valley anisotropy. As discussed in Sec. 2 the L valley states, Eq. (1), transform according to Γ_4^- and Γ_4^+ irreducible representation of the wave vector group D_{3d} in conduction and valence bands, respectively. Therefore in the direct product $\Gamma_4^-\otimes\Gamma_4^+ = \Gamma_1^-\oplus\Gamma_2^-\oplus\Gamma_3^-$ there are two one-dimensional, Γ_1^-, Γ_2^-, and one two-dimensional, Γ_3^- irreducible representations, each corresponding to an exchange constant K_s, K_l and K_t. As a result, the electron-electron representation of the Hamiltonian of the anisotropic intravalley exchange interaction has the following form

$$\hat{H}^{\rm aniso}_{\rm exch} = K_s\frac{\mathbb{1}}{2} - K_t\frac{(\sigma_x^*\sigma_x + \sigma_y^*\sigma_y)}{6} - K_l\frac{(\sigma_z^*\sigma_z)}{6}. \tag{19}$$

Here we used same spin matrices as in Eq. (18). For the known intravalley exchange matrix the exchange constants K_s, K_t and K_l are calculated as

$$K_s = \frac{{\rm Tr}\left(\hat{H}^{\rm aniso}_{\rm exch}\right)}{2}, \quad K_{t(l)} = -\frac{3\,{\rm Tr}\left(M^*_{t(l)}\hat{H}^{\rm aniso}_{\rm exch}\right)}{2}, \tag{20}$$

where $M_t = \sigma_x^*\sigma_x$ or $\sigma_y^*\sigma_y$ and $M_l = \sigma_z^*\sigma_z$. Since the energy of the dark excitons are not shifted by the exchange [33], it is natural to expect that

$$K_s = \frac{2K_t + K_l}{3} \tag{21}$$

and the eigenvalues of $\hat{H}^{\rm aniso}_{\rm exch}$ are

$$E_s = 0, \quad E_t = \frac{K_t + K_l}{3}, \quad E_l = \frac{2K_t}{3}. \tag{22}$$

The intravalley part (19) of the full 64×64 exhcange Hamiltonian can also be calculated via the inverse transformation (11). For the $v \otimes c$ exciton indexing scheme the transformation of exciton states is given by the direct product $U^{v*} \otimes U^c$.

Results of the calculations are shown in Fig. 6 for PbS and in Fig. 7 for PbSe cubic, cuboctahedral and octahedral QDs with tetragonal symmetry. Instead of K_s, K_t, K_l in Figs. 6 and 7 we show $K_s(D)$ and the long range exchange anisotropy parameter

$$\eta_X(D) = \frac{K_l(D) - K_t(D)}{K_s(D)}. \tag{23}$$

Tight-binding data are shown by symbols connected by thin solid lines for each of the three considered shapes of the QDs: cubic by «□», cuboctahedral by «○» and octahedral by «◇». Detailed description of the atomistic structure and shapes of the QDs are given in Ref. [19]. Data calculated within the framework of fully anisotropic **k·p** model [3] are shown by thin dashed lines. One can see that the intravalley exchange is almost insensitive to the shape of the QDs and does not oscillate with the change of the QD diameter. The tight-binding results agree well with anisotropic **k·p** theory. Details of the **k·p** calculations are given in Appendix 4.

The asymptotic values for η_X may be calculated from **k·p** theory [34, 35]. The longitudinal-transverse splitting reads as

$$\hbar\omega_{LT} = \frac{8e^2\hbar^2P^2}{\varepsilon_\infty m_0^2 E_g^2 a_B^3} \tag{24}$$

where a_B is the exciton Bohr radius and ε_∞ is the high frequency dielectric permittivity, see Table 1. It may be shown that the effect of the valley anisotropy may be fully accounted by considering the direction-dependent longitudinal-transverse splitting

$$\hbar\omega^{l(t)}_{LT} = \frac{8e^2\hbar^2P^2_{l(t)}}{\varepsilon_\infty m_0^2 E_g^2 a_B^3}. \tag{25}$$

Table 1. Main components of longitudinal-transverse long range exchange exciton splittings, anisotropic material parameters for bulk PbS and PbSe, high-frequency dielectric permittivity and exciton Bohr radius. $\alpha^b_{t(l)}$ are remote band contributions [3]. Interband momentum matrix elements $P_{t(l)}$ are given in atomic units.

	PbS	PbSe
$\hbar\omega^t_{LT}$ (μeV)	76	19
$\hbar\omega^l_{LT}$ (μeV)	110	11
$\langle\hbar\omega_{LT}\rangle$ (μeV)	87	16
η_X	−0.775	0.689
P_t (atomic)	0.1756	0.2699
P_l (atomic)	0.2110	0.2243
E_g (eV)	0.294	0.213
$\alpha^v_t m_0/\hbar^2$	3.713	3.618
$\alpha^v_l m_0/\hbar^2$	0.481	0.784
$\alpha^c_t m_0/\hbar^2$	3.359	3.006
$\alpha^c_l m_0/\hbar^2$	0.697	0.946
ε_∞ [36]	19.2	26.9
a_B (nm) [37–39]	18	46

Then, the anisotropy of the main components of longitudinal-transverse splitting of the exciton is

$$\eta_X = \frac{\omega^l_{LT} - \omega^t_{LT}}{\langle\omega_{LT}\rangle} = 6\frac{P_t^2 - P_l^2}{2P_t^2 + P_l^2}. \tag{26}$$

The values of η_X for bulk PbS and PbSe are also given in Table 1.

Similarly to the intravalley exchange, Eq. (19), one can also compute the non-diagonal intervalley parts $\hat{H}^{\mu\mu'}_{\rm exch}$, $\mu \neq \mu'$ of the full exchange Hamiltonian. The magnitude of the intervalley exchange in highly symmetric quantum dots is almost identical to the intravalley one $|\hat{H}^{\mu\mu'}_{\rm exch}| \sim |\hat{H}^{\mu\mu}_{\rm exch}|$, so the full exchange Hamiltonian is almost isotropic and also leads to the formation of the ultra-bright valley-symmetric superradiant exciton triplet as was shown in simplified model in Refs. [19] and [27]. However, the intervalley exchange has very complicated non-analytical form and we do not present it here. The only difference with the isotropic approximation is that the valley anisotropy leads to the brightening of some dark triplets. Though, their oscillator strength is still two order of magnitude smaller and the use of isotropic model [19] is fully justified.

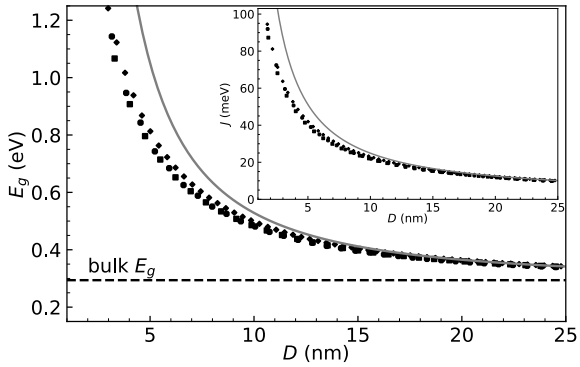

Fig. 8. Main plot: low temperature band gap energy, Eq. (27), as a function of effective diameter in octahedral, cubeoctahedral and cubic PbS QDs. Dashed line indicate the band gap of the bulk PbS. Inset: the upper estimate for the exciton binding energy in PbS QDs. In both plots symbols show the data calculated in tight-binding, solid lines show **k**·**p** results

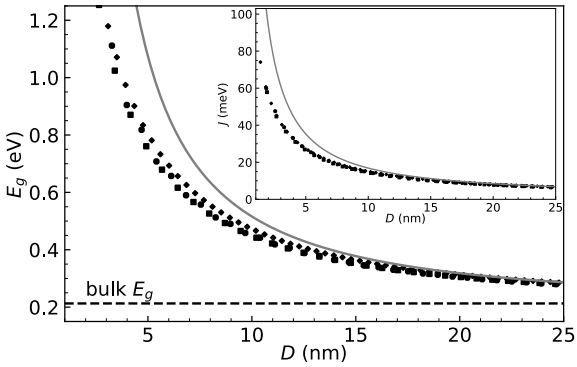

Fig. 9. Same as in Fig. 8, but for PbSe QDs

3.3. Electron and hole energy spectra, exciton binding energies

In this section we discuss energy spectrum of electrons, holes and exciton binding energies in PbX QDs. As mentioned above, in PbX QDs with T_d point symmetry the electron (hole) ground states are split into two doublet levels Γ_6, Γ_7 and a quadruplet Γ_8. Following Ref. [19] we associate the electron (hole) ground confinement energy with the energy of the quadruplet state E_{Γ_8}. This allows to fully parametrize the valley splittings by two energy differences between doublet levels, $E_{\Gamma_6}, E_{\Gamma_7}$, and the quadruplet level E_{Γ_8}. In this notation the band gap energy reads as

$$E_g(D) \equiv E^c_{\Gamma_8}(D) - E^v_{\Gamma_8}(D) \tag{27}$$

and the valley splittings are

$$E^b_{\Gamma_7}(D) - E^b_{\Gamma_8}(D), \quad E^b_{\Gamma_8}(D) - E^b_{\Gamma_6}(D), \quad b = c, v. \tag{28}$$

The band gap energy $E_g(D)$, Eq. (27), is shown in the main plot in Fig. 8 for PbS and in the main plot in Fig. 9 for PbSe QDs. Results of the tight-binding calculations are shown by black symbols. The shapes of the QDs are indicated by the shape of the symbols similar to Figs. 6 and 7. Band gap of the bulk PbS and PbSe crystals, see Table 1, indicated by dashed lines. Solid lines show the band gap calculated in the framework of the **k**·**p** theory in isotropic approximation, see Appendix 4.

Parameters of the valley splittings, Eq. (28), are shown in Fig. 10 for PbS and 11 for PbSe QDs. Due to the fast decay of the valley splitting energies they are shown on logarithmic scale. The shape of QDs in Figs. 10 and 11 are indicated by shape of the symbols and color: red for octahedral, green for cuboctahedral and blue for cubic QDs. Negative values are shown by hollow symbols, positive ones by filled. One can see that the lowest values of the valley splittings are in octahedral QDs, their signs oscillate with the change of the QD size parameter N, see Ref. [19] for details. The largest values of the valley splitting are in cubic QDs, they do not oscillate.

Insets in Figs. 8 and 9 show the estimate for the exciton binding energy $-\hat{J} = J\mathbb{1}$, see Eq. (17), given by the direct Coulomb interaction constant $J > 0$ in PbS and PbSe QDs, respectively. Results of the tight-binding calculations are shown by black symbols. Results of the **k**·**p** calculations are shown by solid lines.

In tight-binding the direct Coulomb is calculated using the same technique with the same high-frequency dielectric constant as for the exchange term. Similar approach is used for **k**·**p** calculations, see details in Appendix 4. This yields the upper estimate for the exciton binding energy since the static dielectric constant ε_0 in PbX is about ten times larger than the high frequency one ε_∞ [36]. One can see that the upper estimate for the exciton binding energy is about an order in magnitude smaller than the effective band gap in PbS and PbSe QDs, which correlates well with the large observed exciton Bohr radii in these materials.

3.4. Valley and exchange exciton splittings

The splitting of the ground exciton level is controlled by the valley mixing $\hat{H}_{VM}$ and long range exchange $\hat{K}$ Hamiltonians (17). Interplay of these two contributions was thoroughly investigated in Ref. [19].

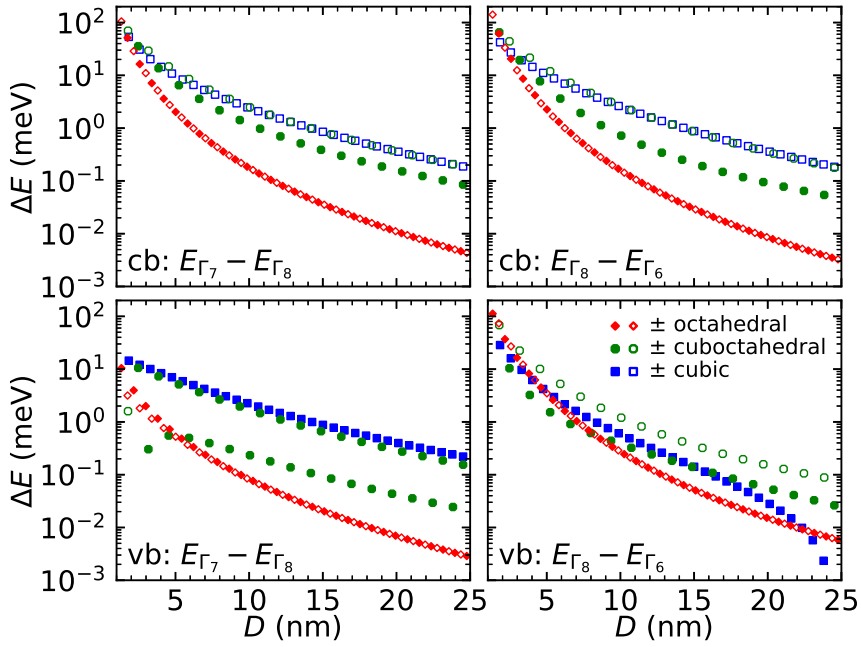

Fig. 10. Valley splitting energies, Eq. (28), in octahedral (red), cuboctahedral (green) and cubic (blue) PbS QDs. Data is shown on logarithmic scale. Filled symbols show positive values of the splitting energies, hollow symbols show negative ones

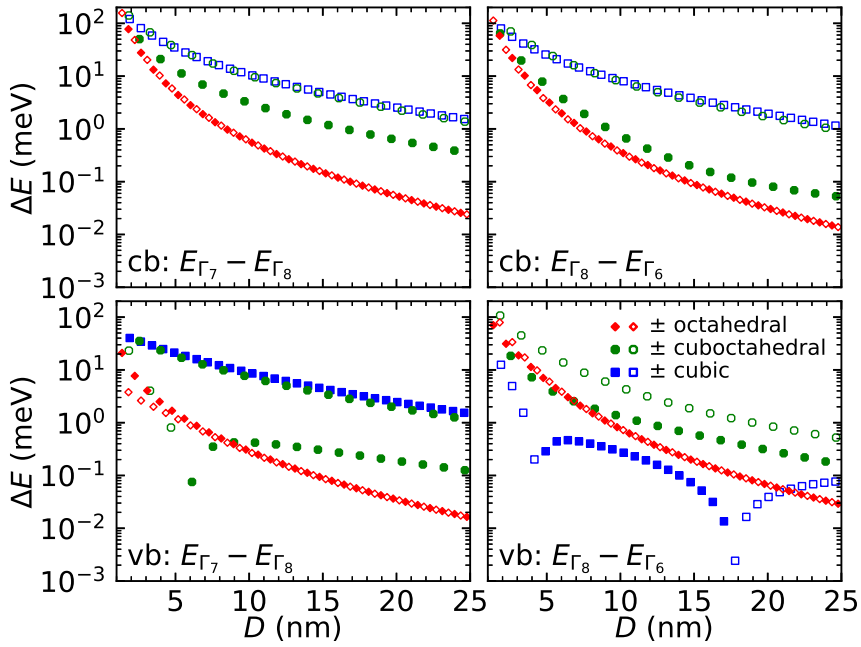

Fig. 11. Same as in Fig. 10, but for PbSe QDs

Here we present the comparison of the two contributions and focus on their scaling as a function of the QD diameter.

The total splitting of the exciton fine structure due to the valley mixing, $\hat{H}_{VM}$, neglecting exchange is given

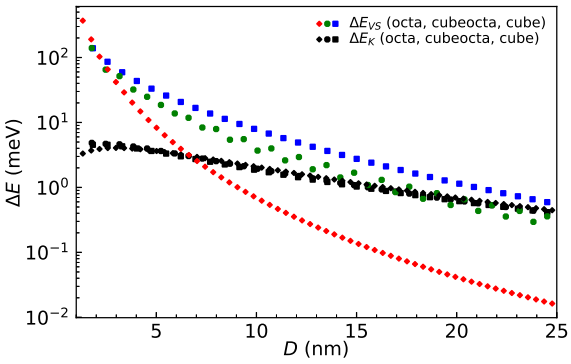

Fig. 12. Total exciton splitting due to the valley mixing of states ΔE_{VS}, Eq. (29), and total exciton exchange splitting ΔE_K, Eq. (30). ΔE_{VS} is shown by color symbols: red for octahedral QDs, green for cuboctahedral QDs and blue for cubic QDs. ΔE_K is shown by black symbols. In both cases the shape of the QDs is also indicated by the shape of the symbols, similarly to Fig. 6

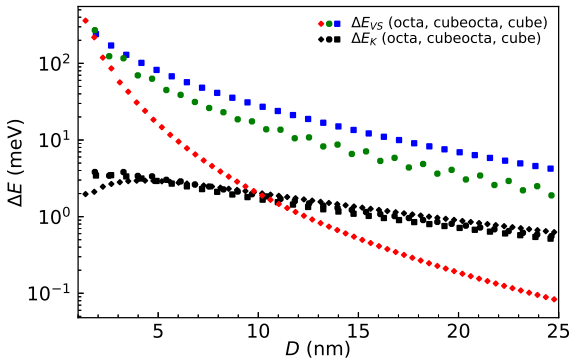

Fig. 13. Same as in Fig. 12, but for PbSe QDs

by distance between furthest exciton levels

$$\Delta E_{VS} = \sum_{b=c,v} \max(E^b_{\Gamma_6}, E^b_{\Gamma_7}, E^b_{\Gamma_8}) - \min(E^b_{\Gamma_6}, E^b_{\Gamma_7}, E^b_{\Gamma_8}). \tag{29}$$

As discussed in Ref. [19], neglecting the valley mixing, the exchange Hamiltonian $\hat{K}$ leads to the formation of the ultra-bright exciton triplet split by

$$\Delta E_K = \frac{8K_s}{3} \tag{30}$$

from the manifold of the dark exciton levels, where K_s is the averaged (isotropic) intravalley exchange constant, see Eq. (21). Due to the cubic (T_d) symmetry of the considered QDs, the exchange Hamiltonian $\hat{K}$ does not split the exciton triplets despite the pronounced anisotropy of the intravalley exchange constants. However, the internal valley anisotropy of the exchange constant leads to the brightening of another exciton triplet to up to about 1% of the oscillator strength of the ultra-bright exciton triplet. This effect is expected to be more pronounced in anisotropic PbX QDs.

The splittings of the exciton level due to the valley mixing, Eq. (29), and exchange Coulomb interaction, Eq. (30), are shown in Fig. 12 for PbS and in Fig. 13 for PbSe QDs. The total valley splitting ΔE_{VS} strongly depend on the shape of the QD and shown by red, green and blue color symbols for octahedral, cuboctahedral and cubic QDs, respectively. The total exchange splitting ΔE_K is almost insensitive to the shape of QDs and shown by black symbols. One can see that in cubic and cuboctahedral QDs the total valley splitting is larger than the exchange one for all range of the computed QD diameters. Therefore in these QDs the exciton fine structure is mostly defined by the valley mixing of states. In octahedral QDs the valley splitting decays much faster. Therefore in small octahedral QDs the exciton fine structure is mostly defined by the valley mixing of states, while in large octahedral QDs the exciton fine structure is dominated by long range exchange interaction.

4. CONCLUSIONS

To conclude, we developed a generalized procedure which allows us to restore the valley states in nanostructures of multivalley semiconductors starting from the quantum confined electron/hole states obtained in atomistic calculations. The method allows for the extraction of the parameters of effective Hamiltonians and/or observables in the physically transparent basis and makes it possible for the direct mapping of the results of atomistic calculations to simplified analytical models.

To demonstrate the strength of the procedure we directly extract the anisotropic exchange constants in PbS and PbSe faceted (cubic, cuboctahedral and octahedral) QDs from the empirical tigh-binding calculations and compared the results to the fully anisotropic **k·p** model. We also showed that in PbSe the intravalley exchange interaction, as well as the intravalley velocity, is almost isotropic, while in PbS it is strongly anisotropic with its longitudinal part being close to zero.

The developed procedure does not depend on particular symmetry, periodicity or valley composition of states of the considered nanostructure and therefore can be applied for any atomistic calculations (including density functional theory) of any multivalley semiconductor nanostructure.

Acknowledgments. Authors thank S.V. Goupalov, M.M. Glazov and E.L. Ivchenko for fruitful discussions. The work of IDA was supported by Russian Science Foundation under grant no. 22-72-00121. IDA also thanks the Foundation for Advancement of Theoretical Physics and Mathematics «BASIS».

APPENDIX A. SYMMETRIZATION

Let $\boldsymbol{\mathcal{E}} = (\chi_1, \chi_2, \ldots, \chi_d)$ be the basis of an irreducible representation Γ of a finite group G of size N, which transforms $\forall g \in G$ as $g\chi_i = \chi_j T_{ji}(g)$ or $g\boldsymbol{\mathcal{E}} = \boldsymbol{\mathcal{E}} T(g)$ and V be a unitary matrix. Then $\boldsymbol{\mathcal{E}}' = \boldsymbol{\mathcal{E}} V$ also forms the basis of the same irreducible representation, but transforms $\forall g \in G$ as $g\boldsymbol{\mathcal{E}}' = \boldsymbol{\mathcal{E}}' D(g)$, where

$$\forall g \in G: \; D(g) = V^{-1} T(g) V \,. \tag{31}$$

Lemma: If $D(g)$ and $T(g)$ matrices are known, then the matrix V can be calculated as

$$V_n = \alpha\, e^{i\frac{2\pi n}{d}} \frac{\tilde{V}}{\det\left(\tilde{V}\right)^{\frac{1}{d}}}, \tag{32}$$

$$\tilde{V} = \sum_{g\in G} T(g) U D(g^{-1}) \,.$$

Here d is the dimension of the representation Γ, α is a common phase multiplier, $|\alpha| = 1$, and U is a matrix with one or several ones. Additional phase $\exp(i2\pi n/d)$ and index $n = 0, \ldots, d-1$ are added explicitly to underline the uncertainty of the root of the complex determinant.

Proof. Consider the matrix $D(g)V^{-1}\tilde{V}$, $g \in G$. Substituting $\tilde{V}$ from Eq. (32) we obtain

$$D(g)V^{-1}\tilde{V} = D(g) \sum_{g'} V^{-1} T(g') U D(g'^{-1}). \tag{33}$$

Now using Eq. (31) and expanding g'^{-1} as $(gg')^{-1}g \equiv g''^{-1}g$ we transform Eq. (33) to

$$V^{-1} \sum_{g''} T(g'') U D(g''^{-1}) D(g) = V^{-1} \tilde{V} D(g). \tag{34}$$

Following the Shur's lemma [40] the matrix $V^{-1}\tilde{V}$ is proportional to the unit matrix and its trace equals to

$$\mathrm{Tr}\left(V^{-1}\tilde{V}\right) = N\,\mathrm{Tr}\left(V^{-1}U\right).$$

Since V is unitary, then V^{-1} has at least one nonzero element $V^{-1}_{ik} \neq 0$. Let $U_{jl} = \delta_{jk}\delta_{il}$, then

$$\mathrm{Tr}\left(V^{-1}U\right) = \sum_{l,j} V^{-1}_{lj} U_{jl} = V^{-1}_{ik} \neq 0.$$

Therefore $\tilde{V} \propto V$, $\det\tilde{V} \neq 0$ and V_n is unitary matrix satisfying Eq. (31). Notice the proof is very similar to the proof of the great orthogonality theorem [40, 41].

The unknown matrix U can be found numerically simply by searching through all d^2 square matrices with one nonzero element. The phase multiplier α is chosen to adjust the time inversion symmetry given by the complex conjugation operator $\hat{K}$. Indeed, let $\hat{K}\boldsymbol{\mathcal{E}} = \boldsymbol{\mathcal{E}} K$, then

$$\hat{K}\boldsymbol{\mathcal{E}}' = \boldsymbol{\mathcal{E}}' V^{-1} K V^* \equiv \boldsymbol{\mathcal{E}}' K'$$

and the matrix

$$K' \propto \alpha^{*2}.$$

The phase $\exp(i2\pi n/d)$ should also be adjusted. The sum over the group elements (32) assumes either sum over double group [24] or use of projective representations [40]. In calculations, it is more convenient to sum over all different matrices which can be obtained from the set of matrices of the generators of the group G, which gives the same result.

Equation (32) can be generalized for projective representations

$$V_n \propto \tilde{V}\,, \quad \tilde{V} = \sum_{r\in F_{\mathbf{k}}} \frac{T(r) U D(r^{-1})}{\omega(r^{-1}, r)}, \tag{35}$$

where r are rotations of the point group F and $\omega(r, r')$ is the factor system of the irreducible representation [40]. Notice ω must be the same for T and D matrices, which can be achieved via bringing both ω_T and ω_D to the standard form. The proof of Eq. (35) is similar, except the following property of the factor system should be used

$$\omega\left((rr')^{-1}, rr'\right) = \frac{\omega(r'^{-1}, r')\omega((rr')^{-1}, r)}{\omega(r, r')}\,. \tag{36}$$

This is general property of the factor system [40]

$$\omega(h_1, h_2h_3)\omega(h_2, h_3) = \omega(h_1h_2, h_3)\omega(h_1, h_2)\,, \tag{37}$$

where

$$h_1 = (rr')^{-1}, \quad h_2 = r, \quad h_3 = r'.$$

Formulae Eqs. (32) and (35) can be applied also for reducible representations such as $\Gamma_{i_1} \oplus \Gamma_{i_2} \ldots \oplus \Gamma_{i_N}$ with no repetitive irreducible ones in the sum. Otherwise the Shur's lemma breaks and other techniques should be used. However, this problem is not typical for tight-binding or other atomistic methods, since in most cases each energy level corresponds to single irreducible representation and accidental degeneracies are extremely rare.

APPENDIX B. INTERCHANGE OF BASIS FUNCTIONS

Let $\Gamma = \bigoplus_{i=1}^{n} \Gamma_m$ be a reducible representation of a group G consisting of n repetitive equivalent irreducible representations Γ_m of size m. Let

$$\boldsymbol{\mathcal{E}} = (\underbrace{\boldsymbol{\mathcal{E}}^1_m, \boldsymbol{\mathcal{E}}^2_m, \ldots, \boldsymbol{\mathcal{E}}^n_m}_{n}), \quad i \neq j \implies \boldsymbol{\mathcal{E}}^i_m \neq \boldsymbol{\mathcal{E}}^j_m\,, \tag{38}$$

be its basis which transforms under $g \in G$ as

$$g\boldsymbol{\mathcal{E}} = \boldsymbol{\mathcal{E}} D(g) \equiv \boldsymbol{\mathcal{E}} \mathbb{1}_n \otimes D_m(g) \tag{39}$$

and has time reversal symmetry

$$\hat{K}\boldsymbol{\mathcal{E}} = \boldsymbol{\mathcal{E}}^* T \equiv \boldsymbol{\mathcal{E}} \mathbb{1}_n \otimes T_m(g). \tag{40}$$

Here $\mathbb{1}_n$ is the $n \times n$ unit matrix.

The basis (38) is not unique. Indeed, consider an interchange of basis functions

$$\boldsymbol{\mathcal{E}}' = \boldsymbol{\mathcal{E}} U \tag{41}$$

given by a matrix U. To satisfy Eqs. (39) and (40) the new basis should be i) orthonormal $\boldsymbol{\mathcal{E}}'^{\dagger}\boldsymbol{\mathcal{E}}' = \mathbb{1}$ and should transform under $g \in G$ and $\hat{K}$ by the same matrices ii) $g\boldsymbol{\mathcal{E}}' = \boldsymbol{\mathcal{E}}' D(g)$ and iii) $\boldsymbol{\mathcal{E}}'^{*} = \boldsymbol{\mathcal{E}}' T$. These conditions constrain the matrix U to: i) $U^{\dagger}U = \mathbb{1}$, ii) $\forall g \in G : D(g)U = UD(g)$ and iii) $UT = TU^*$. Due to the Schur's lemma [40] and the structure of the transformation matrices $D(g) = \mathbb{1}_n \otimes D_m(g)$ the matrix U matrix is a direct product $U_n \otimes \mathbb{1}_m$ of $n \times n$ matrix U_n and the $m \times m$ unit matrix $\mathbb{1}_m$. Since $T = \mathbb{1}_n \otimes T_m$ the third condition $UT = TU^*$ requires $U_n \in O(n)$ to be real orthogonal matrix.

For practical realization we construct the U_n matrix as a product of $n(n-1)/2$ Givens rotation matrices $R_{ij}(\phi)$ [42] and a matrix of phases P which sets the signs of the basis functions:

$$U_n = P \prod_{i<j} R_{ij}(\tilde{\phi}_{ij}) \text{ or } U_n = \left(\prod_{i<j} R_{ij}(\tilde{\phi}_{ij}) \right) P\,, \tag{42}$$

where

$$\tilde{\phi}_{ij} = \pm\phi_{ij}$$

and

$$P = \mathrm{diag}(1, p_2, \ldots, p_n)\,, \quad p_i = \pm 1\,. \tag{43}$$

Nonzero matrix elements of $R_{ij}(\phi)$ are

$$[R_{ij}(\phi)]_{kk} = 1, k \neq i, j,$$

$$[R_{ij}(\phi)]_{ii} = [R_{ij}(\phi)]_{jj} = \cos(\phi),$$

$$[R_{ij}(\phi)]_{ji} = -[R_{ij}(\phi)]_{ij} = \sin(\phi).$$

APPENDIX C. COULOMB INTEGRALS IN ANISOTROPIC k·p

To calculate the intravalley exchange anisotropy in **k·p** we use the anisotropic model and formalism proposed in Ref. [3]. We consider spherical QDs with infinite boundary conditions. The anisotropic **k·p** Hamiltonian is expanded into three terms

$$\hat{H}^{\mathrm{aniso}} = \hat{H}^{\mathrm{iso}} + \delta\hat{H}_P + \delta\hat{H}_\alpha\,, \tag{44}$$

where $\hat{H}^{\mathrm{iso}}$ is the isotropic part of the Hamiltonian, $\delta\hat{H}_P$ accounts for the anisotropy of the interband momentum matrix elements and $\delta\hat{H}_\alpha$ accounts for the anisotropic far-band contributions to the effective masses, see Ref. [3] for details.

Eigenstates of $\hat{H}^{\mathrm{aniso}}$ are expanded over finite basis of the solutions of the isotropic Hamiltonian $\hat{H}^{\mathrm{iso}}$

$$\Psi^{\mathrm{aniso}}_s = \sum_{p=1}^{N} C^s_p \Psi^{\mathrm{iso}}_p \tag{45}$$

and the coefficients C are found via diagonalization of the full $N \times N$ matrix $\hat{H}^{\mathrm{aniso}}_{qp}$. Here indices q, p enumerate both valence and conduction band states. The isotropic wave functions [3]

$$\Psi^{\mathrm{iso}} \equiv |F, p, n, F_z\rangle = \begin{pmatrix} f_{F-\frac{p}{2},p}(r)\,\hat{\Omega}^{F-\frac{p}{2}}_{F,F_z} \\ ipg_{F+\frac{p}{2},p}(r)\,\hat{\Omega}^{F+\frac{p}{2}}_{F,F_z} \end{pmatrix} \tag{46}$$

are bispinors characterized by four quantum numbers: total angular momentum F, its projection F_z, $p = \pm 1$ and main quantum number n which enumerates the roots of dispersion equation. $\hat{\Omega}$ are spherical spinors. The parity of bispinor (46) is given by $\pi = (-1)^{F+\frac{p}{2}}$ To catch the exchange anisotropy in our calculations we limit ourselves with two ground confinement levels per band for each $F = 1/2$ and $3/2$ ($N = 24$ states total).

Using the ansatz (45) the exchange matrix elements [19] become sums of integrals on $\Psi^{\mathrm{iso}}_p \equiv |p\rangle$

$$H^X_{ia,jb} = \sum_{pqrs=1}^{N} C^{j*}_p C^{a*}_q C^b_r C^i_s \langle pq|rs\rangle \tag{47}$$

which are evaluated numerically. The total number of integrals scales as N^4, which is 331776 for $N = 24$.

To reduce the number of integrals to compute we utilize the angular selection rules and employ the index permutation symmetry. For a general four-index Coulomb integral $\langle pq|rs\rangle$ there is particle permutation symmetry $\langle pq|rs\rangle = \langle qp|sr\rangle$, and $\langle pq|rs\rangle = \langle rq|ps\rangle = \langle ps|rq\rangle$ if the matrix elements are

real. In our case the matrix elements are real therefore one has to compute only the matrix elements which satisfy one of the following inequalities:

$$\left[\begin{array}{l} p \le r \le q \le s\,, \\ p < r \le s < q\,, \\ p \le q < r \le s\,, \\ p < q \le s < r\,, \\ p \le s < r \le q\,, \\ p < s < q < r\,. \end{array}\right. \tag{48}$$

These inequalities reduce the number of double integrals to be evaluated for Eq. (57) up to four times. Combined with angular symmetry the total number of different integrals reduces to 298.

The explicit form of the exchange integral (47) is

$$\langle pq|rs\rangle = \frac{e^2}{\varepsilon_\infty}\int \frac{d\mathbf{x}_1 d\mathbf{x}_2}{|\mathbf{r}_1-\mathbf{r}_2|}\Psi_p^*(\mathbf{x}_1)\Psi_q^*(\mathbf{x}_2)\Psi_r(\mathbf{x}_1)\Psi_s(\mathbf{x}_2), \tag{49}$$

where $\int d\mathbf{x} = \int d\mathbf{r}\sum_\sigma$ is the spatial integral and the sum over the bispinor indices σ. Using the Fourier decomposition of $1/r$ the Coulomb integral (49) reduces to

$$\langle pq|rs\rangle = \int \frac{d\mathbf{k}}{2\pi^2 k^2} I_{pr}(\mathbf{k}) I_{qs}(-\mathbf{k}), \tag{50}$$

where

$$I_{uv}(\mathbf{k}) = \\ = \int d\mathbf{r} e^{i\mathbf{k}\cdot\mathbf{r}}\left(f_u f_v \hat{\Omega}^\dagger_{u,-}\hat{\Omega}_{v,-} + p_u p_v g_u g_v \hat{\Omega}^\dagger_{u,+}\hat{\Omega}_{v,+}\right). \tag{51}$$

Here $f(r), g(r)$ are smooth envelopes, $\hat{\Omega}_\pm \equiv \hat{\Omega}^{F\pm\frac{p}{2}}_{F,F_z}$, are spherical spinors and indices p, q, r, s and u, v denote all four quantum numbers of the isotropic wave functions (46). By introducing [43]

$$\hat{\Omega}^{L_1\,\dagger}_{J_1 M_1}\hat{\Omega}^{L_2}_{J_2 M_2} = \sum_{L=|L_1-L_2|}^{L_1+L_2} W_{L,M_1,M_2} Y_{L,-M_1+M_2}, \tag{52}$$

observing (numerically) that

$$\hat{\Omega}^{J_1+\frac{p_1}{2}\,\dagger}_{J_1 M_1}\hat{\Omega}^{J_2+\frac{p_2}{2}}_{J_2 M_2} = \hat{\Omega}^{J_1-\frac{p_1}{2}\,\dagger}_{J_1 M_1}\hat{\Omega}^{J_2-\frac{p_2}{2}}_{J_2 M_2}, \tag{53}$$

and using the plane wave expansion

$$e^{i\mathbf{k}\cdot\mathbf{r}} = 4\pi\sum_{l=0}^{\infty}\sum_{m=-l}^{l} i^l j_l(kr) Y^*_{l,m}(o_\mathbf{k}) Y_{l,m}(o_\mathbf{r}) \tag{54}$$

we further simplify I_{uv} to

$$I_{uv}(\mathbf{k}) = \\ = \sum_{L=|L_u-L_v|}^{L_u+L_v} 4\pi i^L W_{L,M_u,M_v} Y_{L,-M_u+M_v}(o_\mathbf{k}) J^L_{uv}(k)\,, \tag{55}$$

where $L_u = F_u \pm p_u/2$, $L_v = F_v \pm p_v/2$ and

$$J^L_{uv}(k) = \int_0^R r^2 dr j_L(kr)\left[f_u f_v + p_u p_v g_u g_v\right]. \tag{56}$$

Finally we reduce the Coulomb integral (50) to the sum of double integrals

$$\langle pq|rs\rangle = 8\,\delta_{-M_p+M_r,M_q-M_s}(-1)^{-M_q+M_s}\times \\ \times \sum_{L=L_{\min}}^{L_{\max}} W_{L,M_p,M_r} W_{L,M_q,M_s}\int_0^\infty dk J^L_{pr}(k) J^L_{qs}(k), \tag{57}$$

where the L limits are

$$\begin{aligned} L_{\min} &= \max\left(|L_p - L_r|, |L_q - L_s|\right), \\ L_{\max} &= \min\left(L_p + L_r, L_q + L_s\right). \end{aligned} \tag{58}$$

Now the numerical integration is straightforward.

APPENDIX D. ISOTROPIC K·P MODEL, DIRECT COULOMB INTERACTION

The simplified isotropic variant of the **k·p** model is described in details in supplemental materials for Ref. [19]. It was shown in Ref. [19] that the isotropic model successfully predicts the energy of the ground quadruplet Γ_8 in both bands for both octahedral, cubeoctahedral and cubic PbS QDs. Therefore the model is used here to calculate the band gap energy and exciton binding energy (direct Coulomb interaction constant) for all the considered PbS and PbSe QDs.

Table 2. Isotropic parameters for bulk PbS and PbSe. Momentum matrix elements are given in atomic units. E_g and anisotropic parameters are given in Table 1

	PbS	PbSe
P (atomic)	0.1881	0.2556
$a^v m_0/\hbar^2$	2.635	2.674
$a^c m_0/\hbar^2$	2.472	2.320

Parameters of the isotropic model are obtained via averaging of the anisotropic ones over the solid angle

$$P = \sqrt{\frac{2P_t^2 + P_l^2}{3}}, \quad \alpha^b = \frac{2\alpha_t^b + \alpha_l^b}{3}, \quad b = c, v. \quad (59)$$

These parameters are listed in Table 2.

Following Ref. [3] the conduction (valence) band ground states with projection F_z are

$$|c, F_z\rangle = \left| F = \frac{1}{2}, +1, n = 0, F_z \right\rangle,$$

$$|v, F_z\rangle = \left| \frac{1}{2}, -1, n = 0, F_z \right\rangle,$$

where $|F, p, n, F_z\rangle$ are bispinors (46). The explicit form of conduction (valence) ground bispinors are

$$\Psi^c \equiv \begin{pmatrix} f_c(r)\,\hat{\Omega}^0_{\frac{1}{2},F_z} \\ ig_c(r)\,\hat{\Omega}^1_{\frac{1}{2},F_z} \end{pmatrix},$$

$$\Psi^v \equiv \begin{pmatrix} f_v(r)\,\hat{\Omega}^1_{\frac{1}{2},F_z} \\ -ig_v(r)\,\hat{\Omega}^0_{\frac{1}{2},F_z} \end{pmatrix}.$$

Straightforward calculation of direct Coulomb matrix elements (50) yields

$$J = -E_b > 0,$$

$$J = \frac{2e^2}{\pi\varepsilon_\infty} \int_0^\infty dk I_0^v(k) I_0^c(k), \quad (60)$$

where

$$I_0^b(k) = \int_0^R dr\, r^2 j_0(kr) \left(|f_b|^2 + |g_b|^2 \right), \quad b = c, v. \quad (61)$$

REFERENCES

1. A. L. Efros and L. E. Brus, ACS Nano **15**, 4, 6192 (2021).
2. P. Tamarat, E. Prin, Y. Berezovska, A. Moskalenko, T. P. T. Nguyen, C. Xia, L. Hou, J.-Baptiste Trebbia, M. Zacharias, L. Pedesseau, C. Katan, M. I. Bodnarchuk, M. V. Kovalenko, J. Even, and B. Lounis, Nature Communications **14**, 229 (2023).
3. I. D. Avdeev, S. V. Goupalov, and M. O. Nestoklon, Phys. Rev. B **107**, 035414 (2023).
4. M. O. Nestoklon, K. Erik, D. R. Yakovlev, E. A. Zhukov, M. M. Glazov, M. A. Semina, E. L. Ivchenko, E. V. Kolobkova, M. S. Kuznetsova, and M. Bayer, Nano Lett. **23**, 8218 (2023).
5. J. M. Luttinger and W. Kohn, Phys. Rev. **97**, 869 (1955).
6. P. C. Sercel and K. J. Vahala, Phys. Rev. B **42**, 3690 (1990).
7. A. Zunger, *Quantum Theory of Real Materials,* Kluwer International Series in Engineering and Computer Science **348**, 173 (1996).
8. R. Benchamekh, M. O. Nestoklon, J.-M. Jancu, and P. Voisin, *Semiconductor Modeling Techniques*, Springer Series in Materials Scienc **159**, 19 (2012).
9. P. Hohenberg and W. Kohn, Phys. Rev. B **136**, B864 (1964).
10. W. Kohn and L. J. Sham, Phys. Rev. A **140**, A1133 (1965).
11. T. B. Boykin, G. Klimeck, M. Friesen, S. N. Coppersmith, P. von Allmen, F. Oyafuso, and S. Lee, Phys. Rev. B **70**, 165325 (2004).
12. M. O. Nestoklon, L. E. Golub and E. L. Ivchenko, Phys. Rev. B **73**, 235334 (2006).
13. I. D. Avdeev, Phys. Rev. B **99**, 195303 (2019).
14. S. Liangfeng, J. J. Choi, D. Stachnik, A. C. Bartnik, B.-R. Hyun, G. G. Malliaras, T. Hanrath, and F. W. Wise, Nature Nanotech. **7**, 369 (2012).
15. V. Sukhovatkin, S. Hinds, L. Brzozowski, and E. H. Sargent, Science **324**, 1542 (2009).
16. W. A. Tisdale, K. J. Williams, B. A. Timp, D. J. Norris, E. S. Aydil, and X.-Y. Zhu, Science **328**, 1543 (2010).
17. A. N. Poddubny, M. O. Nestoklon, and S. V. Goupalov, Phys. Rev. B **86**, 03532 (2012).
18. I. D. Avdeev, A. N. Poddubny, S. V. Goupalov, and M. O. Nestoklon, Phys. Rev. B **96**, 08531 (2017).
19. I. D. Avdeev, M. O. Nestoklon, and S. V. Goupalov, Nano Lett. **20**, 8897 (2020).
20. A. Svane, N. E. Christensen, M. Cardona, A. N. Chantis, M. van Schilfgaarde, and T. Kotani, Phys. Rev. B **81**, 24512 (2010).
21. A. C. Bartnik, A. L. Efros, W.-K. Koh, C. B. Murray, and F. W. Wise, Phys. Rev. B **82**, 19531 (2010).
22. S. V. Goupalov, Phys. Rev. B **84**, 03730 (2011).
23. S. V. Goupalov, Nanoscale **15**, 1230 (2023).
24. G. F. Koster, J. O. Dimmock, R. G. Wheeler, and H. Statz, *The Properties of the Thirty-Two Point Groups*, M.I.T. Press, Cambridge (1963).

25. J. O. Dimmock and G. B. Wright, Phys. Rev. A **135**, 821 (1964).

26. I. Kang and F. W. Wise, J. Opt. Soc. Am. B **14**, 1632 (1997).

27. S. V. Goupalov, E. L. Ivchenko and M. O. Nestoklon, Phys. Rev. B **106**, 12530 (2022).

28. P.-O. Löwdin, J. Chem. Phys. **18**, 365 (1950).

29. A. M. Abdel-Rehim, R. B. Morgan, D. A. Nicely, and W. Wilcox, SIAM J. Sci. Comp. **32**, 129 (2010).

30. M. O. Nestoklon, R. Benchamekh, and P. Voisin, J. Phys.: Condens. Matter **28**, 30580 (2016).

31. E. L. Ivchenko and M. O. Nestoklon, JETP **94**, 644 (2002).

32. I. D. Avdeev, M. O. Nestoklon, and S. V. Goupalov, Nano Lett. **22**, 7751 (2022).

33. S. V. Goupalov, P. Lavallard, G. Lamouche, and D. S. Citrin, Fiz. Tverd. Tela **45**, 730 (2003).

34. S. V. Gupalov, E. L. Ivchenko, and A. V. Kavokin, JETP **86**, 388 (1998).

35. S. V. Gupalov and E. L. Ivchenko, Phys. Sol. State **42**, 2030 (2000).

36. J. N. Zemel, J. D. Jensen and R. B. Schoolar, Phys. Rev. A **140**, 330 (1965).

37. I. Moreels, K. Lambert, D. Smeets, D. De Muynck, T. Nollet, J. C. Martins, F. Vanhaecke, A. Vantomme, C. Delerue, G. Allan, and Z. Hens, ACS Nano **3**, 3023 (2009).

38. F. W. Wise, Acc. Chem. Res. **33**, 773 (2000).

39. E. Lifshitz, M. Bashouti, V. Kloper, A. Kigel, M. S. Eisen, and S. Berger, Nano Lett. **3**, 857 (2003).

40. G. L. Bir and G. E. Pikus, *Symmetry and Strain-Induced Effects in Semiconductors*, Wiley (1974).

41. A. Zee, *Group theory in a nutshell for physicists*, Princeton Univ. Press (2016).

42. D. S. Matteson and R. S. Tsay, J. Amer. Stat. Association **112**, 623 (2017).

43. D. A. Varshalovich, A. N. Moskalev, and V. K. Khersonskii, *Quantum Theory of Angular Momentum*, World Scientific (1988).